Effect of Nonuniform Flexibility on Hydrodynamic Performance of Pitching Propulsors

Samane Zeyghami[1]
Department of Mechanical Engineering and Mechanics,
Lehigh University,
Bethlehem, PA 18015
e-mail: saz316@lehigh.edu

Keith W. Moored
Department of Mechanical Engineering and Mechanics,
Lehigh University,
Bethlehem, PA 18015
e-mail: kmoored@lehigh.edu

Many aquatic animals propel themselves efficiently through the water by oscillating flexible fins. These fins are, however, not homogeneously flexible, but instead their flexural stiffness varies along their chord and span. Here, we develop a simple model of these functionally graded materials where the chordwise flexibility of the foil is modeled by one or two torsional springs along the chord line. The torsional spring structural model is then strongly coupled to a boundary element fluid model to simulate the fluid–structure interactions. We show that the effective flexibility of the combined fluid–structure system scales with the ratio of the added mass forces acting on the passive portion of the foil and the elastic forces defined by the torsional spring hinge. Importantly, by considering this new scaling of the effective flexibility, the propulsive performance is then detailed for a foil with a flexible hinge that is actively pitching about its leading edge. The scaling allows for the resonance frequency of the fluid–structure system and the bending pattern of the propulsor to be independently varied by altering the effective flexibility and the location of a single torsional spring along the chord, respectively. It is shown that increasing the flexion ratio, by moving the spring away from the leading edge, leads to enhanced propulsive efficiency, but compromises the thrust production. Proper combination of two flexible hinges, however, can result in a gain in both the thrust production and propulsive efficiency. [DOI: 10.1115/1.4041976]

1 Introduction

Flying and swimming animals propel themselves rapidly and efficiently through a fluid using flexible propulsors. A substantial line of work has already confirmed that flexible propulsors are advantageous to rigid ones in aquatic locomotion, specifically with regard to propulsive efficiency [1–4]. Some have argued that the interactions between the fluid and the structure deform the foil in the direction of the fluid. These deformations lead to curvature-induced thrust increases [5] as well as a favorable phase lag between the pitching and heaving motions of the foil, which in return enhances propulsive efficiency [6,7]. In addition, the occurrence of resonance is argued to play an important role in enhancing propulsive performance of flexible foils. Previous studies have shown that the efficiency is maximized at or near the resonance frequency of the combined fluid–structure system [3,4,8]. The resonance frequency of the combined system is a function of the inertial properties of the structure as well as the added mass arising from inertia of the fluid. However, when the flexibility is variable along the chord, the scaling of the resonance frequency of the fluid–structure system is nontrivial, a topic that we will attend to in this study.

The propulsive appendages of swimming and flying animals are made of functionally graded materials where the flexibility varies both along the chord and span. In fact, Combes and Daniel [9] measured the flexural stiffness of several insect wings and found that it declines sharply from the wing base to wing tip, in the spanwise direction, and from the leading edge to the trailing edge, in the chordwise direction. Similarly, the flexibility of the propulsive surfaces of swimming animals (such as fluke, fin, and tail) appears to be nonuniform and declines from the leading to trailing edge and from the center to the edges [10–12]. Inspired by these observations, a number of recent studies have suggested that the distribution of the flexibility along the foil, in addition to its overall flexibility, may play an important role in enhancing the propulsive performance. Comparing different distributions of flexibility along a two-dimensional thin foil undergoing small amplitude heaving motions, Moore [13] has suggested that the concentration of the flexibility at the leading edge enhances thrust production. In another study, Riggs et al. [14] have tested the thrust production of a flexible fin with a standard NACA0012 cross-sectional shape alongside fins with stiffness profiles mimicking that of a Pumpkinseed Sunfish. They showed that biomimetic fins generate more thrust regardless of the overall stiffness of the fin, showing that the performance improvement is due to the stiffness profile itself and not the flexibility alone. Similar conclusions were found by Kancharala and Philen [12] in an experimental study on the propulsive performance of robotic fins with variable chordwise flexibility. They found that fins with variable flexibility outperformed the fins with uniform flexibility with regard to both thrust production and propulsive efficiency.

Here, we aim to probe the effect of the distribution of flexibility on the propulsive performance of a pitching foil by separating the effect of the overall flexibility of a pitching foil from that of its bending pattern. We model the chordwise flexibility of the foil with a series of torsional springs with varying flexibility. The effect of the bending patterns is modeled via changing the location of the spring along the chord. First, we investigate the propulsive performance of a pitching foil with a single flexible joint. We detail the effect of both the overall flexibility and the bending pattern of the foil. Next, we repeat our numerical experiment on a pitching foil with two flexible joints. This time the location of the flexible joints is fixed but the distribution of the flexibility is varied. This study is a primary step toward understanding the role of the functionally graded materials on the propulsive performance. The results of this study can also inspire design of innovative and nontraditional propulsors.

2 Problem Definition

All the numerical experiments are performed on a two-dimensional foil where the leading edge of the foil is actively pitching with a peak-to-peak amplitude of $2\theta_0 = 10$ deg. There are either one or two flexible joints along the chord modeled by torsional springs (Fig. 1). The distance of the flexible joint from the

[1]Corresponding author.

Contributed by the Fluids Engineering Division of ASME for publication in the Journal of Fluids Engineering. Manuscript received February 5, 2018; final manuscript received November 2, 2018; published online February 8, 2019. Assoc. Editor: Olivier Coutier-Delgosha.

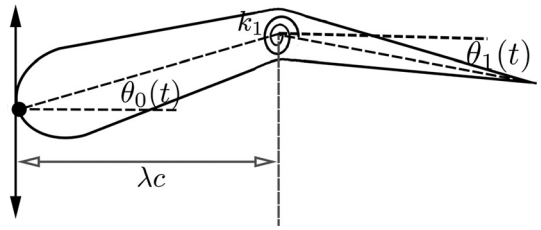

Fig. 1 Schematic of the model for a single spring

leading edge, normalized by the chord length, is quantified by the flexion ratio, λ. The flapping frequency and swimming velocity are kept constant across these simulations at 2.87 Hz and 0.1 m/s resulting in a reduced frequency of $k = 2.87$ (defined as $k = fc/U$) for a chord length of $c = 0.1$ m, and a Strouhal number (defined as $\mathrm{St} = fA/U$) of 0.5. This St is defined for a rigid foil without a flexible joint. However, the real St of the flow is an output of the system and varies with the trailing edge amplitude, which itself is a function of the flexibility and flexion ratio.

For materials with similar densities as those of the surrounding fluid (in the present study $\rho_s = \rho$), the flexibility of the combined fluid–structure system is a function of the added mass forces of the fluid and the elastic forces of the structure. We define Π_k as the ratio of these forces, which characterizes the *effective flexibility* of the combined fluid–structure system

$$\Pi_k = (1-\lambda^2)\sqrt{\frac{\rho b c^4 f^2}{k_\theta}} \tag{1}$$

where ρ, f, c, and k_θ, respectively, are the fluid density, pitching frequency, chord length, and the spring stiffness. The numerator is the added mass force represented as a cylinder of fluid with a diameter equal to length of the passive portion of the foil multiplied by a characteristic acceleration. When only added mass forces are modeled, Π_k is directly proportional to the ratio of the driving and resonance frequencies.

Both flexibility and flexion ratio are changed, and their effect on the propulsive performance is detailed. The performance is analyzed using thrust and power coefficients as well as the propulsive efficiency, which are defined below:

$$C_t = \frac{T}{0.5\rho U^2 bc}, \quad C_p = \frac{P}{0.5\rho U^3 bc} \tag{2}$$

where T and P are the time-averaged thrust and input power, and b is the span length that is set to unity. P is calculated by integrating the fluid moment generated by each body panel about the leading edge multiplied by the angular rate of the leading edge. Alternatively, we normalized thrust and power with the added mass forces as defined in Eq. (3). Note that the trailing edge amplitude is an output of a flexible foil system

$$C_t' = \frac{T}{0.5\rho A^2 f^2 bc}, \quad C_p' = \frac{P}{0.5\rho U A^2 f^2 bc} \tag{3}$$

where A is the trailing edge peak-to-peak amplitude.

3 Numerical Methods

The flow over the foil is modeled using a two-dimensional potential flow method where the flow is assumed to be irrotational, incompressible, and inviscid. We follow Refs. [15] and [16], in that the general solution to the potential flow problem is reduced to finding a distribution of doublets and sources on the foil surface and in the wake that satisfies a no-flux boundary condition on the body at each time-step. Constant strength source and doublet line elements are distributed over the body and the wake. Each body boundary element is assigned a collocation point, which is shifted a small distance under the body surface (here 1% of the local thickness of the body). The constant potential Dirichlet condition is enforced at the collocation points to ensure a no-flux boundary condition on the body surface. Additionally, at each time-step a wake boundary element is shed with a strength that is set by applying an explicit Kutta condition, where the vorticity at the trailing edge is set to zero [17–19]. A wake rollup algorithm is employed to ensure that the wake does not support any force. The wake elements advect by the local velocity at the wake panel edge points. During the wake rollup, the point vortices, representing the ends of the wake doublet elements, must be de-singularized for numerical stability of the solution [20]. To do so, at a small cutoff radius of $\epsilon = 0.05c$, the irrotational induced velocities from the point vortices are replaced by a rotational Rankine core model. The tangential perturbation velocity component is calculated by local differentiation of the perturbation potential. Finally, the pressure acting on the body is found via applying the unsteady Bernoulli equation. More details can be found in Refs. [15,21,22].

The structural flexibility is modeled via torsional springs, which connect the structural mesh elements together. The kinematics of the leading structural element is always prescribed. The following equation governs the dynamics of the passive structural elements

$$\mathbf{I}\ddot{\Theta} + \mathbf{C}\dot{\Theta} + \mathbf{K}_\theta \Theta = \mathbf{N}_f + \mathbf{N}_i + \mathbf{N}_h \tag{4}$$

where $\mathbf{N}_f$ is the hydrodynamic moment exerted about the flexible joint location, $\mathbf{N}_i$ is the inertial moment due to the translational velocity of the center of mass of the corresponding element, $\mathbf{N}_h$ is the moment exerted by the forces at the joint, which keep the elements together, $\mathbf{I}$ is the matrix of moments of inertia about the joint locations, and $\mathbf{K}_\theta$ and $\mathbf{C}$ are the matrices of the structural stiffness and damping, respectively. Also, Θ is a vector containing the orientation of the passive elements. For a foil with two flexible joints, we have

$$\mathbf{I} \equiv \begin{bmatrix} I_1 & 0 \\ 0 & I_2 \end{bmatrix} \quad \mathbf{K}_\theta \equiv \begin{bmatrix} k_{\theta_1} + k_{\theta_2} & -k_{\theta_2} \\ -k_{\theta_1} & k_{\theta_2} \end{bmatrix} \quad \mathbf{C} \equiv \begin{bmatrix} c_1 + c_2 & -c_2 \\ -c_1 & c_2 \end{bmatrix} \tag{5}$$

where I_i is the moment of inertia of the ith element, and c_i and k_{θ_i} are the structural damping and the stiffness of the spring attached to the leading edge of the ith element.

To solve the fluid–structure interaction problem, Eq. (4) is discretized in time, using the trapezoidal rule (Eqs. (6) and (7)), and solved within each small time-step via a strong coupling between the fluid and structural solvers, which is accelerated by the Aitken method. To improve the convergence properties of the solver, while keeping its efficiency, we use two different time-step sizes Δt and Δt_s for the fluid and structure solvers, respectively, where $\Delta t_s = \Delta t / N_s$. N_s is set to 100 in the present simulations

$$\hat{\Theta}^{m+1} = \hat{\Theta}^m + \frac{1}{2}\left(\dot{\hat{\Theta}}^m + \dot{\hat{\Theta}}^{m+1}\right)\Delta t_s \tag{6}$$

$$\dot{\hat{\Theta}}^{m+1} = \dot{\hat{\Theta}}^m + \frac{1}{2}\left(\ddot{\hat{\Theta}}^m + \ddot{\hat{\Theta}}^{m+1}\right)\Delta t_s \tag{7}$$

where superscripts m and $m+1$ represent the values at times t_s^m and t_S^{m+1}, respectively, and $\hat{x}$ represents any variable x within the structure solver. Substituting Eq. (7) into Eq. (6) and solving for $\ddot{\Theta}^{m+1}$, we get

$$\ddot{\hat{\Theta}}^{m+1} = \left(\frac{2}{\Delta t_s}\right)^2 \left(\hat{\Theta}^{m+1} - \hat{\Theta}^m\right) - \left(\frac{4}{\Delta t_s}\right)\dot{\hat{\Theta}}^m - \ddot{\hat{\Theta}}^m \tag{8}$$

Similarly, Eq. (6) can be rearranged to get an expression for $\dot{\hat{\Theta}}^{m+1}$ as a function of $\hat{\Theta}$

$$\dot{\hat{\Theta}}^{m+1} = \frac{2}{\Delta t_s}\left(\hat{\Theta}^{m+1} - \hat{\Theta}^m\right) - \dot{\hat{\Theta}}^m \tag{9}$$

where the right-hand sides of both Eqs. (8) and (9) are known from the previous iteration.

Substituting Eqs. (9) and (8) into Eq. (4), we can rewrite the governing equations as a linear, but coupled, system of equations as follows:

$$A\hat{\Theta}^{m+1} = \hat{b}^m$$

$$A = K_\theta + \left(\frac{2}{\Delta t_s}\right)^2 I + \left(\frac{2}{\Delta t_s}\right) C$$

$$\hat{b}^m = \left(\frac{2}{\Delta t_s}\right)^2 I\hat{\Theta}^m + \left(\frac{4}{\Delta t_s}\right) I\dot{\hat{\Theta}}^m + I\ddot{\hat{\Theta}}^m + \left(\frac{2}{\Delta t_s}\right) C\hat{\Theta}^m + C\dot{\hat{\Theta}}^m + \hat{N}_i^m + \hat{N}_f^m + \hat{N}_h^m \tag{10}$$

Equation (10) together with Eqs. (6) and (7) forms a complete set of equations for the structure. The set of structure equations are first initialized by the known solution from the previous time-step (of the fluid's solver) and then iterated N_s times to advance the solution as much as Δt. To improve convergence, Eq. (10) is uncoupled by employing a Gauss–Seidel formulation where the newly obtained solution for the orientation of the first element is used to obtain the solution for the second element at each time-step t_s.

The Aitken acceleration method is commonly used in the numerical simulation of fluid–structure interactions and is proven to be sufficiently simple and efficient [23–25]. This method uses the values from the two previous iterations to correct the new solution. We employ Aitken's method to advance the solution in the fluid's solver based on the residual calculated in the previous two iterations. The residual is calculated as the difference in the solution obtained in the structure and the fluid solvers, $\mathbf{r}_i = \hat{\Theta}_i - \Theta_i$, where Θ_i is a vector representing the orientation of the neutral axis of the foil in the fluid solver.

The solution to the coupled fluid–structure system at each time-step $t_n = n\Delta t$ is obtained by following the algorithm below:

(1) $i = 0$, $r_0 = 1$, $\tilde{\Theta}_0 = \Theta_{n-1}$, $\dot{\tilde{\Theta}}_0 = \dot{\Theta}_{n-1}$, $\ddot{\tilde{\Theta}}_0 = \ddot{\Theta}_{n-1}$, and $\omega_0 = 1e-2$.
(2) While $\|r_i\| > \delta$
  (a) $i = i+1$.
  (b) If $i > 1$, modify the solution; $\tilde{\Theta}_i = \tilde{\Theta}_{i-1} + \omega_{i-1} r_{i-1}$.
  (c) Calculate the location of the neutral axis of the foil in the fluid solver via known values of the leading element and passive elements.
  (d) Calculate the position and velocity of the fluid panels on the foil surface.
  (e) Calculate fluid forces and moments.
  (f) Solve the solid deformations; $\hat{\Theta}_i$, $\dot{\hat{\Theta}}_i$, and $\ddot{\hat{\Theta}}_i$ using Eqs. (10), (8), and (7).
  (g) Calculate the residual, $r_i = \hat{\Theta}_i - \tilde{\Theta}_i$.
  (h) Calculate Aitken acceleration factor;
    if $i < 3$, $\omega_i = \omega_0$.
    else, $\omega_i = \omega_{i-1}(\mathbf{r}_{i-1} - \mathbf{r}_i)/\|r_{i-1} - r_i\|^2)$.
(3) Update the solution for time t_n; $\Theta_n = \tilde{\Theta}_i$, $\dot{\Theta}_n = \dot{\tilde{\Theta}}_i$, and $\ddot{\Theta}_n = \ddot{\tilde{\Theta}}_i$.

where δ is set to 10^{-8}. When the solution converges within the nth time-step, we set $n = n+1$ and repeat the steps above to solve for the next time-step.

3.1 Discretization Independence. Figure 2 shows propulsive efficiency as a function of number time steps within an oscillation period, N_t, and number of body panels, N_p. The leading edge kinematics and the St are set to the same values as the main case studies. λ and Π_k are set to 0.8 and 0.3, respectively. $\Pi_k = 0.3$ marks the resonance frequency of the flow–structure system. It is evident that η converges to the discretization independent solutions as the number of body panels and time steps increases. The efficiency changes by less than 4% when $N_{\text{panel}} = 700$ and $N_{\text{time}} = 800$ are doubled.

3.2 Validation. We tested the accuracy of our numerical model by comparing our results against the analytical results presented in Ref. [26] for a two-dimensional thin foil with a torsional spring at the leading edge. A small amplitude (harmonic) heaving motion is enforced at the leading edge. The foil passively pitches about the leading edge due to the action of fluid, inertial, and elastic forces. We compared both the cycle-averaged thrust and the cycle-averaged power with the analytical solution. The results are shown in Fig. 3.

4 Results and Discussion

4.1 Single Flexible Joint. Figure 4(*a*) shows the nondimensional trailing edge amplitude, $A^* = A/A_{\text{rigid}}$, as a function of effective flexibility for five different flexion ratios. The trailing edge amplitude is maximum at the resonance, which occurs at $\Pi = 0.3$ for all flexion ratios. The coincidence of the resonance frequency for all λ shows that the proposed scaling for the effective flexibility appropriately accounts for the effect of the flexion ratio. However, inspecting the trend of variations in A^* with Π_k reveals that the effective damping of the combined fluid–structure system increases for larger λ values. It is also worth noting that before and after resonance, higher flexion ratio foils generally experience larger trailing edge amplitude. For flexion ratios smaller than 0.5, the trailing edge amplitude increases with λ. This relationship is reversed for $\lambda > 0.5$.

Figure 4(*b*) shows variations in thrust and power coefficients as a function of Π_k. Unlike the trailing edge amplitude, the thrust coefficient is generally larger for small λ rather than large values,

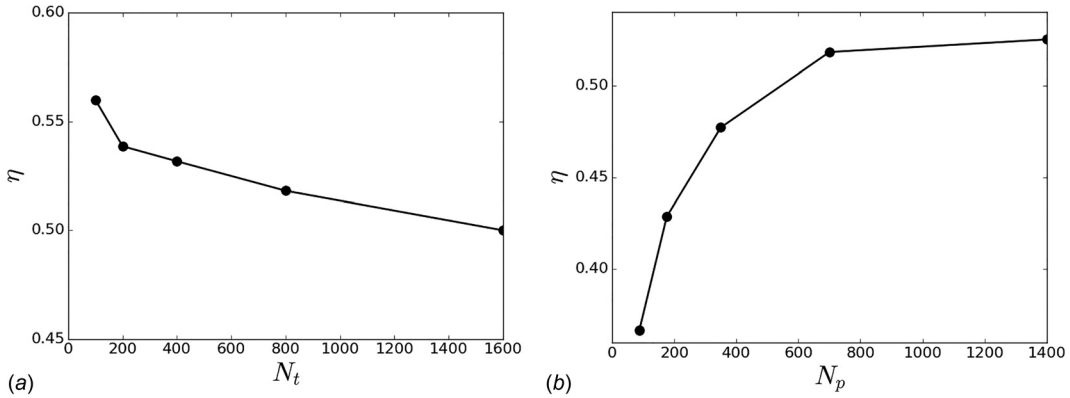

Fig. 2 Propulsive efficiency as a function of (*a*) number of time steps and (*b*) number of body panels

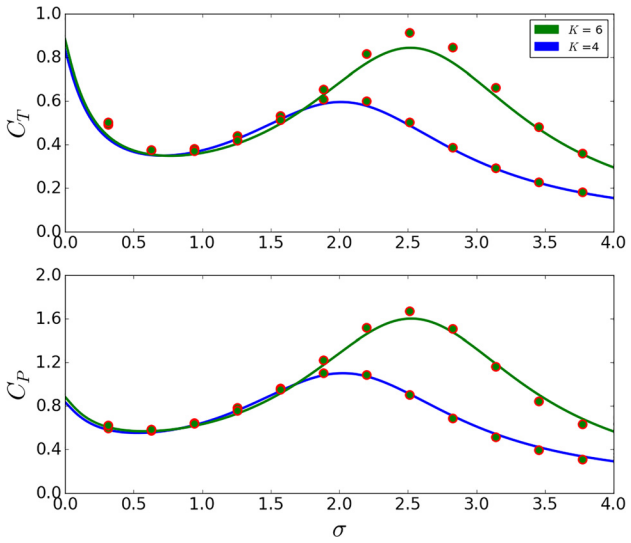

Fig. 3 Analytical solutions for thrust and power coefficient as a function of reduced frequency, for two different nondimensional spring stiffnesses, are shown with solid lines. These solutions are taken from Ref. [26]. Closed circles are the solutions calculated by the present numerical method.

except for very rigid foils where increasing λ up to 0.5 results in a gain in thrust. Inspecting Fig. 4(*c*) shows that this gain in thrust comes with no additional cost with regard to the power consumption. C_t rises up to its peak value at the resonance, for small λ values, and then drops quickly with further increase in flexibility. This is unlike the behavior of C_t for large λ values where the thrust plateaus before resonance and then drops with a mild slope when flexibility increases. It is worth noting that for all flexion ratios, C_t increases faster than C_p until slightly after resonance. This is reflected in Fig. 4(*d*) where we show changes in the propulsive efficiency, defined as $\eta = C_t/C_p$, as a function of Π_k. There is a sharp drop in thrust production after the resonance for small λ values, which results in a decline in the propulsive efficiency. In contrast, for large flexion ratios, η keeps increasing with flexibility for a wide range of flexibilities.

In Figs. 5(*a*) and 5(*b*), we plotted C_t' and C_p' as the function of Π_k. When we normalized the thrust by the trailing edge velocity, the peak in the force production and power consumption disappeared implying that the peak is merely a consequence of the amplified trailing edge amplitude. Variations in the trailing edge amplitude are responsible for the major changes in the thrust production for $\lambda = 0$. However, this is not the case for other λ values. The fact that the curves for different λ values do not collapse on top of one another implies that the bending pattern itself, and not only the trailing edge amplitude, plays a role in the force production.

The behavior of the C_p' curves is somewhat different from that of C_t'. Before resonance, the power coefficient appears to drop sharply by increasing flexibility. After the resonance, for small λ values, the power coefficient starts to rise again. This results in a drop in efficiency, which is due to a simultaneous rise in power consumption and drop in thrust production. For larger λ values, however, as flexibility increases, C_p' keeps declining where the rate of this decline decreases for large flexibilities. Thus, the rate of increase in efficiency with Π_k (Fig. 4(*d*)) decreases.

To summarize our findings with regard to the propulsive performance of these flexible foils, we plotted contours of C_t' and C_p'

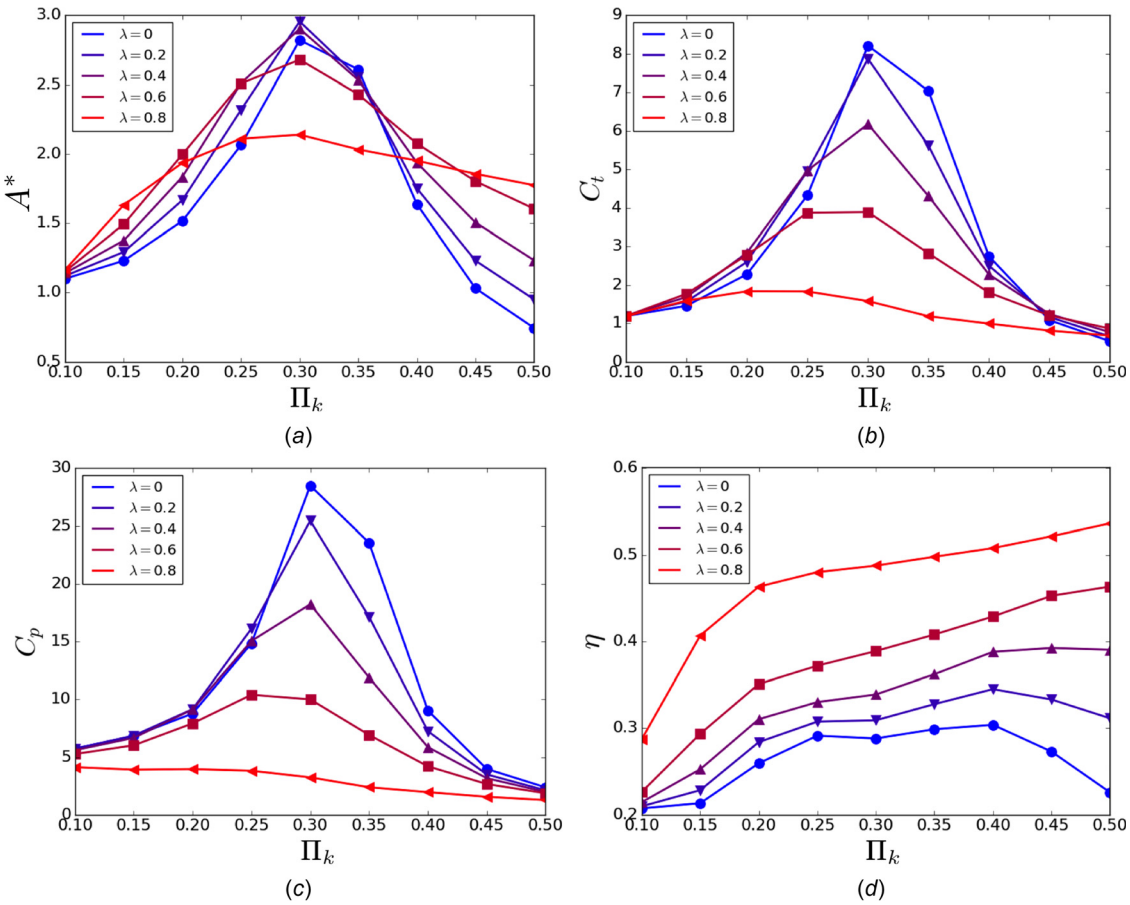

Fig. 4 (*a*) Trailing edge amplitude, (*b*) thrust coefficient, (*c*) power coefficient, and (*d*) efficiency as a function of Π_k

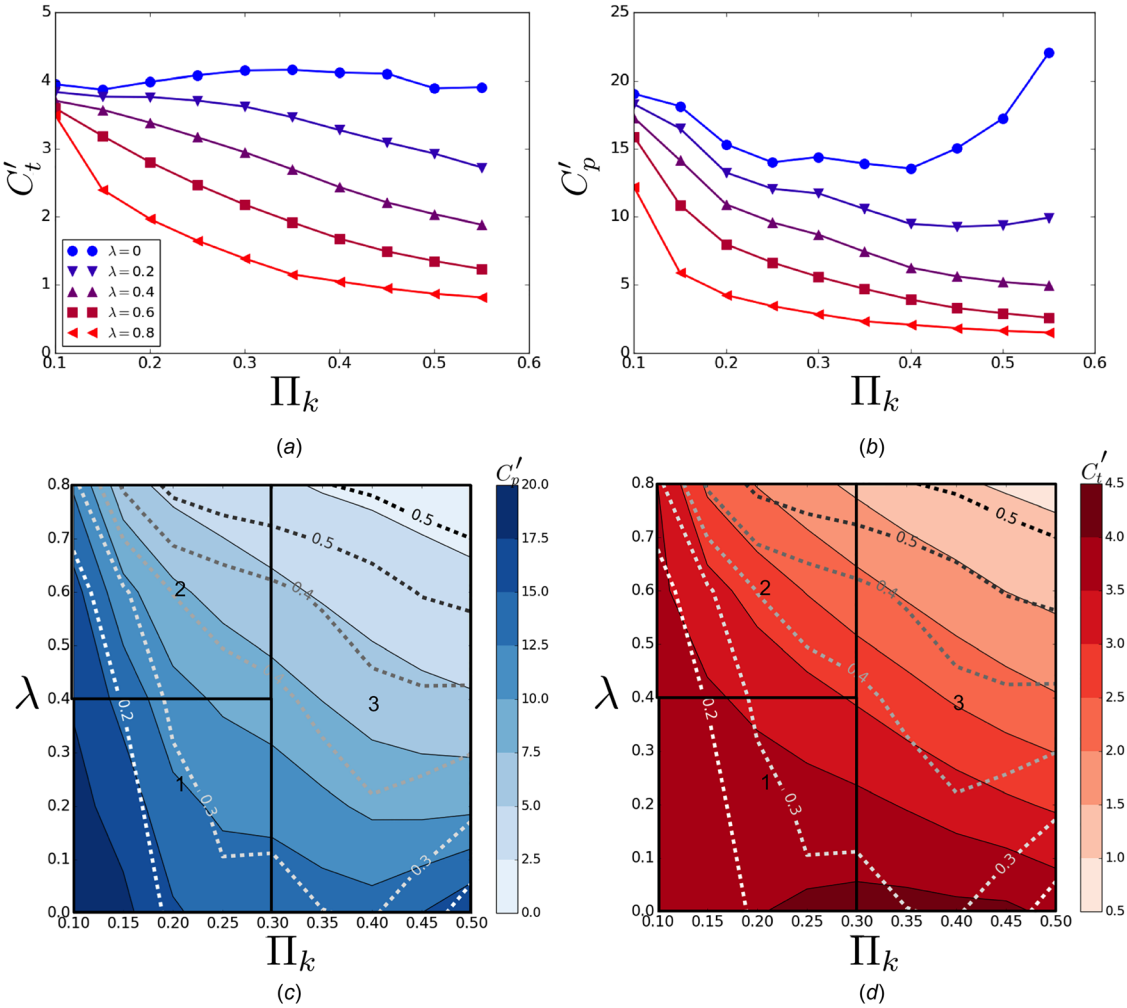

Fig. 5 Variation of thrust (*a*) and power (*b*) coefficients, C_t' and C_p', defined by Eq. (3) with Π_k. Contours of C_t' and C_p' in λ–Π_k plane. Dotted lines are the contours of propulsive efficiency.

as a function of λ and Π_k in Figs. 5(*c*) and 5(*d*). Contours of propulsive efficiency are overlaid on both figures with dotted lines. It is worth noting that the contours of efficiency line up with those of power consumption indicating that the propulsive efficiency is mostly governed by the input power requirement and not the thrust production. We identified three regions on these contour plots. In region 1, which contains low Π_k and low λ value foils, the thrust coefficient remains relatively constant. The propulsive efficiency can be enhanced by increasing flexibility (contours of propulsive efficiency are almost parallel to the λ-axis). In region 2, increasing either flexibility or flexion ratio benefits efficiency but compromises thrust production. In region 3, contours of power consumption, and thus propulsive efficiency, are more or less aligned with the Π_k axis, meaning that the efficiency is more sensitive to changing the flexion ratio. Thus, implying that for largely flexible foils, increasing the flexion ratio can result in improved propulsive performance.

4.2 Two Flexible Joints. In Sec. 4.1, we showed that changing the bending patterns of a pitching foil via increasing its flexion ratio is the key to improving the propulsive efficiency. However, there is a tradeoff to this gain since smaller flexion ratios are required for larger force production. We hypothesize that combining multiple flexible joints may be the key to gaining both in efficiency and thrust magnitude. To test our hypothesis, we repeated our numerical experiment on a pitching foil with two torsional springs located half a chord away from each other at $\lambda_1 = 0.2$ and $\lambda_2 = 0.7$. The kinematics of the leading edge was kept identical to the cases studied in Sec. 4.1.

When multiple flexible joints are allowed, not only the flexibility of the individual joint but also the profile of flexibility distribution along the chord will affect the foil's deformations and, thus, its propulsive performance. Here, we chose a profile that maintains the effective flexibility of the foil unchanged along the chord (keeping Π_k identical for the two springs). The spring stiffness, thus, declines quadratically with the normalized distance from the leading edge, $k \propto (\lambda - 1)^4$. To do so, the stiffness of each one of the springs is determined solely based on its distance from the leading edge using Eq. (1).

Figure 6(*a*) shows the trailing edge amplitude as a function of Π_k. A foil with two flexible joints has two resonances; however, only one is captured in this figure. The resonance occurs at Π_k of 0.35, which is slightly larger than the resonance Π_k for each individual flexible joint. This could be due to increased circulatory effects or existence of nonlinear added mass effects when combining the two joints. In comparison to one flexible joint configurations, the trailing edge amplitude of the present configuration reaches a higher maximum at the resonance, and drops slower afterward. The deformation of the middle element appears to be maximum at the resonance (Fig. 7). However, the amplitude of the motion of the last element continues to increase after the resonance attenuating the drop in trailing edge amplitude.

In Fig. 6(*b*), the left axis shows the cycle-averaged thrust coefficients, C_t. Similar to the results in Sec. 4.1, the peak thrust generation occurs at the resonance but the magnitude of the peak is

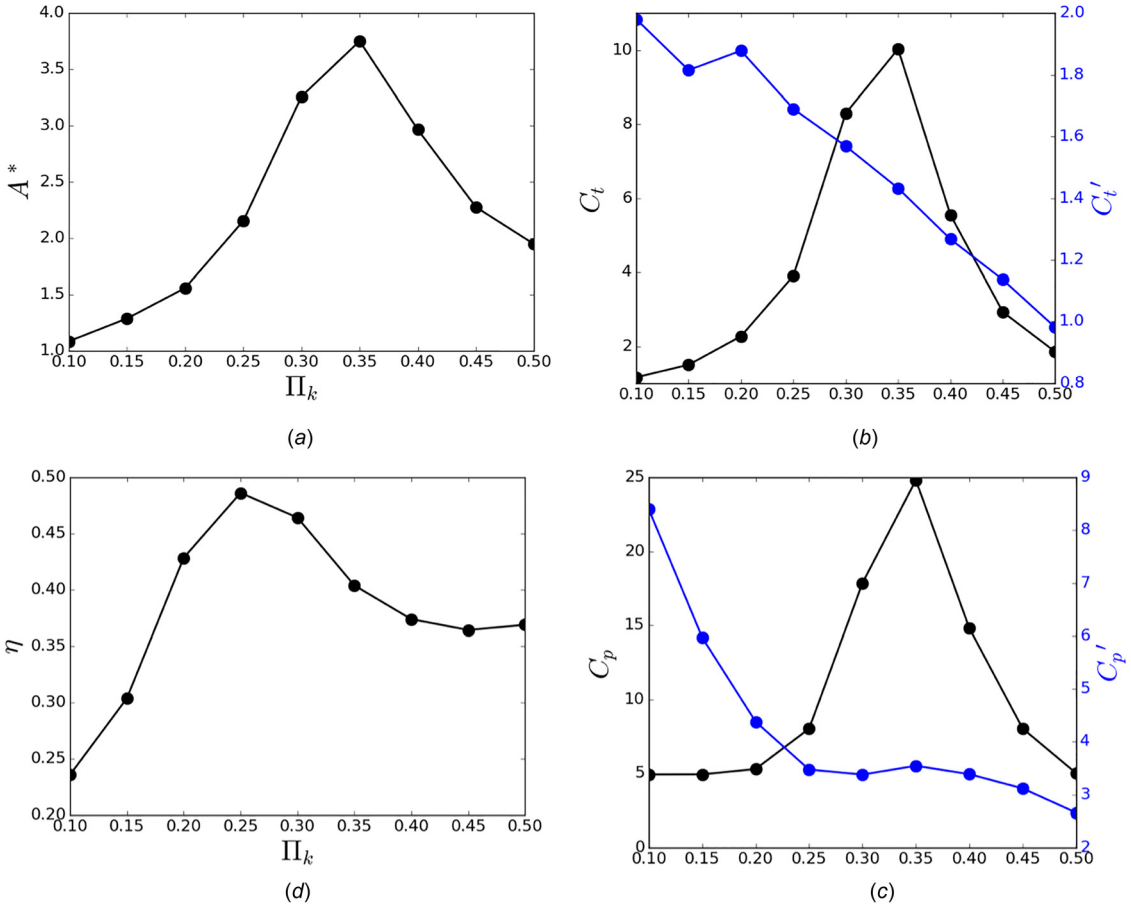

Fig. 6 (*a*) Trailing edge amplitude, (*b*) thrust coefficient, (*c*) power coefficient, and (*d*) efficiency as a function of Π_k for two flexible hinge configuration

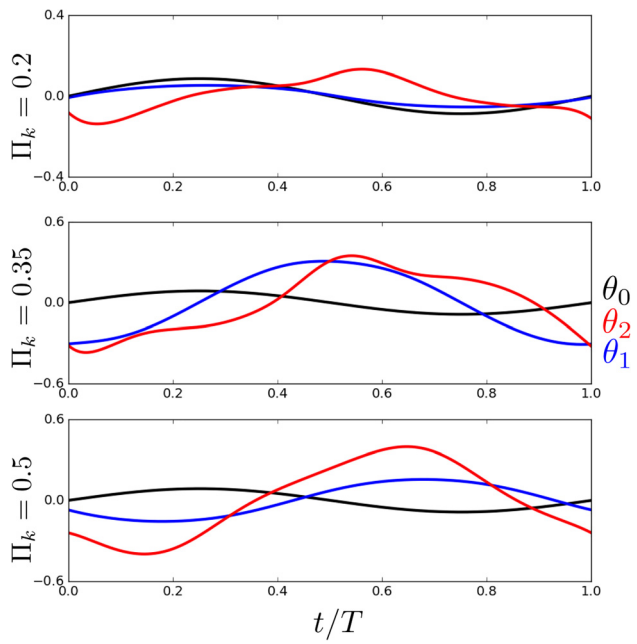

Fig. 7 Change in the relative orientation of the solid elements versus time, within one cycle. The line representing θ_0 shows the prescribed pitching motion of the leading edge. The lines representing θ_1 and θ_2, respectively, show the deflection angles of the second and the third element. The deflection angles are measured relative to the preceding element. The angles are shown for three different Π_k values of 0.2, 0.35, and 0.5.

substantially higher. This is partially due to the increased trailing edge amplitude, which leads to enhanced added mass forces and a favorable reorientation of the hydrodynamic force relative to the propulsive direction. For $\Pi_k \leq 0.3$, the magnitude of C_t is similar to that of a foil with a single flexible joint at $\lambda = 0.2$ indicating that the effect of the combination of the two joints was not destructive to the thrust production capacity. For larger flexibilities, C_t is larger than what was achieved by any of the single jointed foil configurations due to the constructive combination effect. In the same figure, the right axis shows C_t' where thrust is normalized by the trailing edge velocity rather than the swimming velocity. Similar to the case of a single spring, C_t' drops with increasing flexibility.

Unlike thrust, the power coefficient, C_p, remains small for small Π_k values (Fig. 6(*c*)). This results in a quick rise in the propulsive efficiency of the double jointed foil, as reflected in Fig. 6(*c*). In the same figure, the right axis shows C_p'. This curve shows a fast drop in the power consumption with flexibility before the resonance (which is typical of high flexion ratio foils in single spring configurations), where at $\Pi_k \geq 0.25$, the power coefficient is already below what was achieved by most of the single spring configurations (Fig. 5). C_p' continues to drop even more so after resonance. In such a way, the two-spring configuration maintains high propulsive efficiency and thrust production across a wide range of flexibilities spanning both sides of resonance. Overall, the results of this section support our earlier hypothesis.

5 Conclusions

Here, we proposed an effective flexibility scaling that allows resonance frequency of the fluid–structure system and its bending pattern to be independently varied. In addition, we proposed a

systemic approach to studying the effect of the distribution of flexibility across the chord line of flexible foils. Using this new scaling, it has been shown that the unsteady propulsive performance of flexible foils with a single torsional spring hinge is not only a function of their effective flexibility but also their bending patterns. Across all flexibilities tested here, increasing flexion ratio was beneficial to the efficiency while diminishing the thrust production. We showed that the combined effect of the flexibility and the flexion ratio can result in propulsive efficiencies as large as 50% or more for a purely pitching foil. This is more than five times larger than the propulsive efficiency of a rigid foil with the same leading edge kinematics.

Additionally, flexible foils with two flexible joints were examined to probe whether multiple flexible hinges could be used to attenuate the tradeoff between thrust and efficiency to achieve fast and efficient swimming simultaneously. The flexibility of the joints was determined such that the effective flexibility was constant along the chord. We found that this combination of flexible joints has a constructive effect on the propulsive performance of a pitching foil with regard to both thrust and efficiency across a wide range of flexibilities.

Finally, it is important to note that the fluid–structure model used in this study is subject to several assumptions. The fluid model, for instance, does not account for viscous effects such as the separation that may occur at the leading edge or along the deforming body, especially when the solid deformation is large. These effects can potentially influence the propulsive performance especially with regard to the power consumption. Future work will address these issues.

Acknowledgment

This work was supported by the Office of Naval Research under Program Director Dr. Robert Brizzolara on MURI Grant No. N00014-08-1-0642 as well as by the National Science Foundation under Program Director Dr. Ronald Joslin in Fluid Dynamics within CBET on NSF Award No. 1653181.

Funding Data

- Office of Naval Research Global (Grant No. N00014-08-1-0642, Funder ID. 10.13039/100007297).

Nomenclature

A = trailing edge amplitude
c = fin chord
C = damping matrix
C_p, C'_p = power coefficient
C_t, C'_t = thrust coefficient
f = pitching frequency
I = matrix of moment of inertia
k = reduced frequency
K = stiffness matrix
N_f = hydrodynamic moment
N_h = hinge moment
N_i = inertial moment
U = swimming velocity
α = there are two arguments for each entry of the nomenclature environment, the symbol, and the definition
λ = flexion ratio
Π_k = effective stiffness
ρ = fluid density

References

[1] Wu, T. Y.-T., 1971, "Hydromechanics of Swimming Propulsion—Part 3: Swimming and Optimum Movements of Slender Fish With Side Fins," J. Fluid Mech., **46**(3), pp. 545–568.
[2] Lighthill, M. J., 1970, "Aquatic Animal Propulsion of High Hydromechanical Efficiency," J. Fluid Mech., **44**(2), pp. 265–301.
[3] Dewey, P. A., Boschitsch, B. M., Moored, K. W., Stone, H. A., and Smits, A. J., 2013, "Scaling Laws for the Thrust Production of Flexible Pitching Panels," J. Fluid Mech., **732**, pp. 29–46.
[4] Masoud, H., and Alexeev, A., 2010, "Resonance of Flexible Flapping Wings at Low Reynolds Number," Phys. Rev. E, **81**(5), p. 56304.
[5] Katz, J., and Weihs, D., 1978, "Hydrodynamic Propulsion by Large Amplitude Oscillation of an Airfoil With Chordwise Flexibility," J. Fluid Mech., **88**(3), pp. 485–497.
[6] Zhu, Q., 2007, "Numerical Simulation of a Flapping Foil With Chordwise or Spanwise Flexibility," AIAA J., **45**(10), pp. 2448–2457.
[7] Quinn, D. B., Lauder, G. V., and Smits, A. J., 2015, "Maximizing the Efficiency of a Flexible Propulsor Using Experimental Optimization," J. Fluid Mech., **767**, pp. 430–448.
[8] Siala, F. F., Totpal, A. D., and Liburdy, J. A., 2016, "Characterization of Vortex Dynamics in the Near Wake of an Oscillating Flexible Foil," ASME J. Fluids Eng., **138**(10), p. 101202.
[9] Combes, S., and Daniel, T., 2003, "Flexural Stiffness in Insect Wings—Part I: Scaling and the Influence of Wing Venation," J. Exp. Biol., **206**(Pt. 17), pp. 2979–2987.
[10] Fish, F., and Lauder, G., 2006, "Passive and Active Flow Control by Swimming Fishes and Mammals," Annu. Rev. Fluid Mech, **38**(1), pp. 193–224.
[11] Bose, N., Lien, J., and Ahia, J., 1990, "Measurements of the Bodies and Flukes of Several Cetacean Species," Proc. R. Soc. B, **242**(1305), pp. 163–173.
[12] Kancharala, A., and Philen, M., 2016, "Optimal Chordwise Stiffness Profiles of Self-Propelled Flapping Fins," Bioinspiration Biomimetics, **11**(5), p. 056016.
[13] Moore, M. N. J., 2015, "Torsional Spring is the Optimal Flexibility Arrangement for Thrust Production of a Flapping Wing," Phys. Fluids, **27**(9), p. 091701.
[14] Riggs, P., Bowyer, A., and Vincent, J., 2010, "Advantages of a Biomimetic Stiffness Profile in Pitching Flexible Fin Propulsion," J. Bionic Eng., **7**(2), pp. 113–119.
[15] Katz, J., and Plotkin, A., 2001, *Low-Speed Aerodynamics*, 2nd ed., Cambridge University Press, New York.
[16] Quinn, D. B., Moored, K. W., Dewey, P. A., and Smits, A. J., 2014, "Unsteady Propulsion Near a Solid Boundary," J. Fluid Mech., **742**, pp. 152–170.
[17] Willis, D. J., 2006, "An Unsteady, Accelerated, High Order Panel Method With Vortex Particle Wakes," Ph.D. thesis, Massachusetts Institute of Technology, Cambridge, MA.
[18] Wie, S. Y., Lee, S., and Lee, D. J., 2009, "Potential Panel and Time-Marching Free-Wake-Coupling Analysis for Helicopter Rotor," J. Aircr., **46**(3), pp. 1030–1041.
[19] Pan, Y., Dong, X., Zhu, Q., and Yue, D. K. P., 2012, "Boundary-Element Method for the Prediction of Performance of Flapping Foils With Leading-Edge Separation," J. Fluid Mech., **698**, pp. 446–467.
[20] Krasny, R., 1986, "Desingularization of Periodic Vortex Sheet Roll-Up," J. Comput. Phys., **65**(2), pp. 292–313.
[21] Moored, K. W., and Quinn, D. B., 2018, "Inviscid Scaling Laws of a Self-Propelled Pitching Airfoil," AIAA J. (epub).
[22] Akoz, E., and Moored, K. W., 2018, "Unsteady Propulsion by an Intermittent Swimming Gait," J. Fluid Mech., **834**, pp. 149–172.
[23] Mok, D. P., and Wall, W., 2001, "Partitioned Analysis Schemes for the Transient Interaction of Incompressible Flows and Nonlinear Flexible Structures," *Trends in Computational Structural Mechanics*, W. A. Wall, K.-U. Bletzinger, and K. Schweizerhof, eds., CIMNE, Barcelona, Spain.
[24] Küttler, U., and Wall, W. A., 2008, "Fixed-Point Fluid-Structure Interaction Solvers With Dynamic Relaxation," Comput. Mech., **43**(1), pp. 61–72.
[25] Borazjani, I., Ge, L., and Sotiropoulos, F., 2008, "Curvilinear Immersed Boundary Method for Simulating Fluid Structure Interaction With Complex 3D Rigid Bodies," J. Comput. Phys., **227**(16), pp. 7587–7620.
[26] Moore, M. N. J., 2014, "Analytical Results on the Role of Flexibility in Flapping Propulsion," J. Fluid Mech., **757**, pp. 599–612.